

262 Latin American Journal of  
263 Solids and Structures

264 **An adaptive continuum/discrete crack approach for meshfree**  
265 **particle methods**

266 T. Rabczuk and T. Belytschko\*

267 Department of Mechanical Engineering, Northwestern University, 2145 Sheridan Road, Evanston, IL  
268 60208-311, U.S.A.

269 Abstract

270 A coupled continuum/discrete crack model for strain softening materials is implemented  
271 in a meshfree particle code. A coupled damage plasticity constitutive law is applied until a  
272 certain strain based threshold value - this is at the maximum tensile stress of the equivalent  
273 uniaxial stress strain curve - is reached. At this point a discrete crack is introduced and  
274 described as an internal boundary with a traction crack opening relation. Within the frame-  
275 work of meshfree particle methods it is possible to model the transition from the continuum  
276 to the discrete crack since boundaries and particles can easily be added and removed. The  
277 EFG method and an explicit time integration scheme is used. The integrals are evaluated  
278 by nodal integration, an integration with stress points and also a full Gauss quadrature.  
279 Some results are compared to experimental data and show good agreement. Additional  
280 comparisons are made to a pure continuum constitutive law.

281 key words: meshfree methods, discrete crack model, concrete, loss of hyperbolicity

282 **1 Introduction**

283 When modelling materials with strain softening, pure continuum based constitutive laws have  
284 difficulties because the loss of hyperbolicity of the PDE results in localization to a set of measure  
285 zero in rate independent materials, see Bazant and Belytschko [4]. The resulting spurious mesh  
286 dependency requires regularization techniques. Within the framework of meshfree methods, it  
287 is easily possible to treat discrete discontinuities, so that it is not necessary to describe the  
288 softening regime within the constitutive model. Hence, the difficulty mentioned above can be  
289 avoided.

290 A softening regime is observed in the macroscopic stress strain curve, i.e. the stresses decrease  
291 with increasing strain, when a material undergoes sufficient damage. Detailed studies (see  
292 e.g. [18, 21]) in brittle materials such as concrete and ceramics have shown that microcracks  
293 are initiated and later form macrocracks. The formation of a visible macrocrack is generally  
294 assumed to occur when the stress strain curve reaches its maximum tensile stress. Because of

---

\* Corresponding author Email: tedbelytschko@northwestern.edu Received 19 Sep 2003; Revised 30 Oct 2003

295 the roughness of the crack edges, traction forces still can be transmitted along the crack close  
 296 to the crack tip until the material separates completely.

297 In continuum based material models, plasticity and/or damage models are applied to repro-  
 298 duce this constitutive behavior. However, difficulties occur with the onset of softening since the  
 299 PDE changes its type. In static problems this leads to the loss of ellipticity, in dynamic problems  
 300 to the loss of hyperbolicity. Several regularization techniques have been developed to avoid this  
 301 shortcoming. In the case of damage models, a viscous damage can be added, so that the hy-  
 302 perbolicity is retained as shown in [27]. Viscoplastic models also avoid the loss of hyperbolicity  
 303 and mesh dependency, see e.g. Belytschko et al. [11], Needleman [22], Loret et al. [3]. A more  
 304 natural way is to treat the macrocrack as a discontinuity. Meshfree particle methods are well  
 305 suited for such approaches since boundaries and particles can be added adaptively quite easily.  
 306 In this paper we will propose a continuum/discrete crack approach within the framework of  
 307 meshfree particle methods based on an adaptive refinement scheme.

308 The article is arranged as follows. First, the EFG method is briefly reviewed. Then the  
 309 weak form of the linear momentum equation will be derived for treating the discontinuity, i.e.  
 310 the crack, as an internal boundary. The discrete crack is modelled via the visibility criterion.  
 311 Its mechanics is described by a traction crack opening model for concrete materials. In section  
 312 3 the combined continuum/discrete crack approaches will be proposed. Implementation details  
 313 are discussed. Finally, the approaches are tested and applied to notched concrete beams under  
 314 quasistatic and dynamic loading. The beams fail because of a mixed mode (mode I-II) fracture.  
 315 Crack patterns and load displacement curves for several beams with different locations of the  
 316 notch are compared to experimental data and show good agreement.

## 317 2 A discrete crack approach in the element free Galerkin method

### 318 2.1 Meshfree approximation

The meshfree MLS-approximation in a Lagrangian description can be written as

$$u(\mathbf{X}, t) = \mathbf{p}^T(\mathbf{X}) \mathbf{a}(\mathbf{X}, t) \quad (1)$$

where  $\mathbf{X}$  are the material coordinates,  $t$  is the time and  $\mathbf{a}$   $\mathbf{p}$  are linear basis functions  $\mathbf{p}(\mathbf{X}) = (1 \ X \ Y) \ \forall \mathbf{X} \in \mathfrak{R}^2$ . Minimizing

$$J = \sum_{I \in S} (\mathbf{p}_I^T(\mathbf{X}) \mathbf{a}(\mathbf{X}, t) - u_I(t))^2 W(\mathbf{X} - \mathbf{X}_I, h) \quad (2)$$

with respect to  $\mathbf{a}$  leads to the approximation

$$u(\mathbf{X}, t) = \sum_{I \in S} \Phi_I(\mathbf{X}) u_I(t) \quad (3)$$

319 where  $\Phi_I(\mathbf{X})$  is the shape function of particle  $I$ ,  $S$  is the set of neighbor particles for  $\mathbf{X}$ ,  $u_I$  is  
 320 the value at the particle at the position  $\mathbf{X}_I$ ,  $W(\mathbf{X} - \mathbf{X}_I, h)$  is a window function and  $h$  is the

321 interpolation radius of the window function. In the EFG-method (see Belytschko et al. [9, 10])  
 322 the shape functions are:

$$\Phi_J = \mathbf{p}^T(\mathbf{X}) \cdot \mathbf{A}(\mathbf{X})^{-1} \cdot \mathbf{B}(\mathbf{X}) \quad (4)$$

$$\mathbf{A}(\mathbf{X}) = \sum_{J \in S} \mathbf{p}_J(\mathbf{X}) \mathbf{p}_J^T(\mathbf{X}) W(\mathbf{X} - \mathbf{X}_J, h) \quad (5)$$

$$\mathbf{B}(\mathbf{X}) = \sum_{J \in S} \mathbf{p}_J(\mathbf{X}) W(\mathbf{X} - \mathbf{X}_J, h) \quad (6)$$

323 Lagrangian kernels, i.e. kernels that are functions of material coordinates, are used in the above  
 324 because of their improved stability properties, see Belytschko et al. [7, 25].

## 325 2.2 The discrete linear momentum equation

Consider a body  $\Omega$  whose undeformed image is  $\Omega_0$  with boundary  $\Gamma_0$ . The strong form of the linear momentum equation is:

$$\nabla \cdot \mathbf{P} + \varrho_0 \mathbf{b} = \varrho_0 \ddot{\mathbf{u}} \text{ in } \Omega_0 \quad (7)$$

and the boundary conditions are

$$\mathbf{n}_0 \cdot \mathbf{P} = \bar{\mathbf{t}}_0 \text{ in } \Gamma_0^t \quad (8)$$

$$\mathbf{u} = \bar{\mathbf{u}} \text{ in } \Gamma_0^u \quad (9)$$

where  $\mathbf{P}$  is the nominal stress,  $\varrho_0$  is the initial density,  $\mathbf{b}$  are the body forces,  $\mathbf{u}$  and  $\ddot{\mathbf{u}}$  are the displacements and accelerations, respectively,  $\mathbf{n}_0$  is the normal to the boundary in the initial configuration and  $\bar{\mathbf{u}}$  and  $\bar{\mathbf{t}}$  denote the applied displacements and tractions, respectively;  $\Gamma_0^u \cup \Gamma_0^t = \Gamma_0$ ;  $\Gamma_0^u \cap \Gamma_0^t = \emptyset$ . The weak form of the linear momentum equation is obtained by multiplying the momentum equation with the test functions  $\delta \mathbf{u}$  and integrating over the domain:

$$\int_{\Omega_0} \nabla \cdot \mathbf{P} \cdot \delta \mathbf{u} \, d\Omega_0 + \int_{\Omega_0} \varrho_0 (\mathbf{b} - \ddot{\mathbf{u}}) \cdot \delta \mathbf{u} \, d\Omega_0 = 0 \quad (10)$$

The first term on the RHS of the momentum equation can be transformed by integration by parts

$$\int_{\Omega_0} \nabla \cdot \mathbf{P} \cdot \delta \mathbf{u} \, d\Omega_0 = \int_{\Omega_0} \nabla \cdot (\mathbf{P} \cdot \delta \mathbf{u}) \, d\Omega_0 - \int_{\Omega_0} (\nabla \otimes \delta \mathbf{u})^T : \mathbf{P} \, d\Omega_0 \quad (11)$$

Using the Gauss theorem, the first term on the RHS of equation (11) can be written as

$$\int_{\Omega_0} \nabla \cdot (\mathbf{P} \cdot \delta \mathbf{u}) \, d\Omega_0 = \int_{\Gamma_0^t} \mathbf{n}_0 \cdot \mathbf{P} \cdot \delta \mathbf{u} \, d\Gamma_0 + \int_{\Gamma_0^{cA}} \mathbf{n}_0^A \cdot \mathbf{P}^A \cdot \delta \mathbf{u}^A \, d\Gamma_0 + \int_{\Gamma_0^{cB}} \mathbf{n}_0^B \cdot \mathbf{P}^B \cdot \delta \mathbf{u}^B \, d\Gamma_0 \quad (12)$$

326 where the second and third term on the right hand side represent the traction at the crack  
 327 boundary as illustrated in figure 1. The crack can be considered as an internal boundary with  
 328 two crack edges as shown in figure 1 with  $\Gamma_0^c = \Gamma_0^{cA} \cup \Gamma_0^{cB}$ .

329 With the relation  $\mathbf{t}_0^A = \mathbf{n}_0^A \cdot \mathbf{P}^A$ ,  $\mathbf{t}_0^B = \mathbf{n}_0^B \cdot \mathbf{P}^B$  and under the assumption that  $\mathbf{n}_0^A = -\mathbf{n}_0^B$ ,  
 330 the weak Galerkin form of the linear momentum equation including a discontinuity is then:

$$\begin{aligned} \int_{\Omega_0} \varrho_0 \delta \mathbf{u} \cdot \ddot{\mathbf{u}} \, d\Omega_0 + \int_{\Omega_0} (\nabla \otimes \delta \mathbf{u})^T : \mathbf{P} \, d\Omega_0 - \int_{\Omega_0} \varrho_0 \delta \mathbf{u} \cdot \mathbf{b} \, d\Omega_0 \\ - \int_{\Gamma_0^t} \delta \mathbf{u} \cdot \bar{\mathbf{t}}_0 \, d\Gamma - \int_{\Gamma_0^{cA}} \mathbf{t}_0^A \cdot \delta \mathbf{u}^A \, d\Gamma_0 - \int_{\Gamma_0^{cB}} \mathbf{t}_0^B \cdot \delta \mathbf{u}^B \, d\Gamma_0 = 0 \end{aligned} \quad (13)$$

Assuming that the traction  $\mathbf{t}_0^A = -\mathbf{t}_0^B$ , the weak form of the linear momentum equation can be written as

$$\begin{aligned} \int_{\Omega_0} \varrho_0 \delta \mathbf{u} \cdot \ddot{\mathbf{u}} \, d\Omega_0 + \int_{\Omega_0} (\nabla \otimes \delta \mathbf{u})^T : \mathbf{P} \, d\Omega_0 - \int_{\Omega_0} \varrho_0 \delta \mathbf{u} \cdot \mathbf{b} \, d\Omega_0 \\ - \int_{\Gamma_0^t} \delta \mathbf{u} \cdot \bar{\mathbf{t}}_0 \, d\Gamma - \int_{\Gamma_0^c} \mathbf{t}_0 \cdot \llbracket \delta \mathbf{u} \rrbracket \, d\Gamma_0 = 0 \end{aligned} \quad (14)$$

331 where  $\delta \mathbf{u} \in V_0$  are the test functions and  $\mathbf{u} \in V_1$  are the trial functions. The same test and trial  
 332 functions are used for  $\delta \mathbf{u}$  and  $\mathbf{u}$ . The spaces  $V_0$  and  $V_1$  are as follows:

$$V_1 = \{ \mathbf{u} \mid \mathbf{u} \in H^1(\Omega), \mathbf{u} \text{ discontinuous on } \Gamma_0^c, \mathbf{u} = \bar{\mathbf{u}} \text{ on } \Gamma_u \} \quad (15)$$

$$V_0 = V_1 \cap \{ \delta \mathbf{u} \mid \delta \mathbf{u} = 0 \text{ on } \Gamma_u \} \quad (16)$$

333 The test and the trial functions are approximated via the following equations:

$$\delta \mathbf{u}^h(\mathbf{X}) = \sum_J \Phi_J(\mathbf{X}) \delta \mathbf{u}_J \quad (17)$$

$$\mathbf{u}^h(\mathbf{X}, t) = \sum_J \Psi_J(\mathbf{X}) \mathbf{u}_J(t) \quad (18)$$

Substituting (17) and (18) into (14) gives

$$\begin{aligned} \sum_I \int_{\Omega_0} \varrho_0 \Phi_J(\mathbf{X}) \Phi_I(\mathbf{X}) \, d\Omega_0 \ddot{\mathbf{u}}_I = \int_{\Omega_0} \varrho_0 \Phi_I \mathbf{b} \, d\Omega_0 + \\ \int_{\Gamma_0^t} \Phi_I \bar{\mathbf{t}}_0 \, d\Gamma_0 + \int_{\Gamma_0^c} \llbracket \Phi_I \rrbracket \bar{\mathbf{t}}_0 \, d\Gamma_0 - \int_{\Omega_0} \nabla \Phi_I \cdot \mathbf{P} \, d\Omega_0 \end{aligned} \quad (19)$$

334 The integrals are evaluated numerically by nodal integration, a combination of nodal integra-  
 335 tion with stress points or a full Gauss quadrature based on a background mesh, see Rabczuk et  
 336 al. [25]. A detailed description how to integrate over the crack domain is given in the following  
 337 sections.

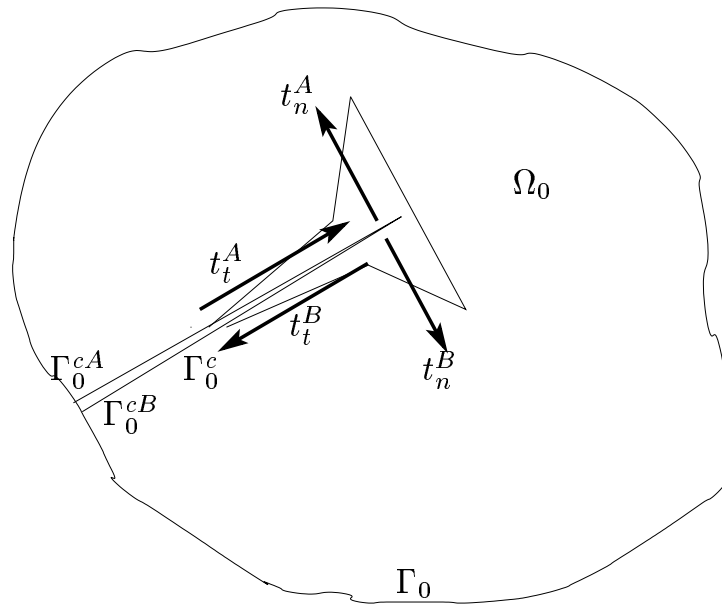


Figure 1: Domain with crack boundary

### 338 2.3 The discrete crack model

According to figure 1 the crack surface integral is:

$$\int_{\Gamma_0^c} \mathbf{t}_0 \cdot \llbracket \delta \mathbf{u} \rrbracket d\Gamma_0 = \int_{\Gamma_0^c} (\mathbf{t}_0^A \cdot \delta \mathbf{u}^A + \mathbf{t}_0^B \cdot \delta \mathbf{u}^B) d\Gamma_0 \quad (20)$$

The traction  $\mathbf{t}_0$  along the boundary  $\Gamma_0^c$  depends on the jump in the displacement  $\llbracket \mathbf{u} \rrbracket$ . Let  $\mathbf{t}_0^A$  be the traction on  $\Gamma_0^{cA}$  and  $\mathbf{t}_0^B$  the traction on boundary  $\Gamma_0^{cB}$  as shown in figure 1; note that  $\mathbf{t}_0^A = -\mathbf{t}_0^B$ . The tractions  $\mathbf{t}_0^A$  and  $\mathbf{t}_0^B$  can be expressed as a function of the jump in the displacement:

$$\mathbf{t}_0^A = \boldsymbol{\tau}_0^A(\llbracket \mathbf{u} \rrbracket) = \boldsymbol{\tau}_0^A(\mathbf{u}^A - \mathbf{u}^B) = -\mathbf{t}_0^B \quad (21)$$

where  $\llbracket \mathbf{u} \rrbracket$  represents the relative displacements between the crack surfaces  $\Gamma_0^{cA}$  and  $\Gamma_0^{cB}$ , i.e. the crack opening and is given by

$$\llbracket \mathbf{u} \rrbracket = \mathbf{u}(\mathbf{X}^A) - \mathbf{u}(\mathbf{X}^B) = \sum_I \Phi_I(\mathbf{X}^A) \mathbf{u}_I - \sum_I \Phi_I(\mathbf{X}^B) \mathbf{u}_I \quad (22)$$

#### 339 2.3.1 Treatment of the discontinuity via the visibility criterion

340 The discontinuity, i.e. the jump in the displacement, is modelled via the visibility criterion.  
 341 Therefore, any node  $J$  is excluded from  $S_{\mathbf{X}_I}$  if the line  $\mathbf{X}_I \bar{\mathbf{X}}_J$  intersects the discontinuity (see  
 342 figure 3 and 2). The LHS of figure 3 shows the continuous one dimensional cubic spline. On the  
 343 RHS we assume a discontinuity at  $x = 1.2$ , where the cubic spline is cut.

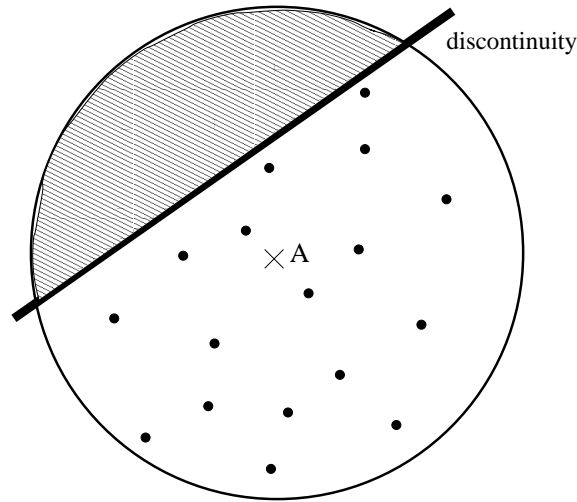


Figure 2: The visibility criterion; shaded area shows the nodes that have no influence on the approximation at point A

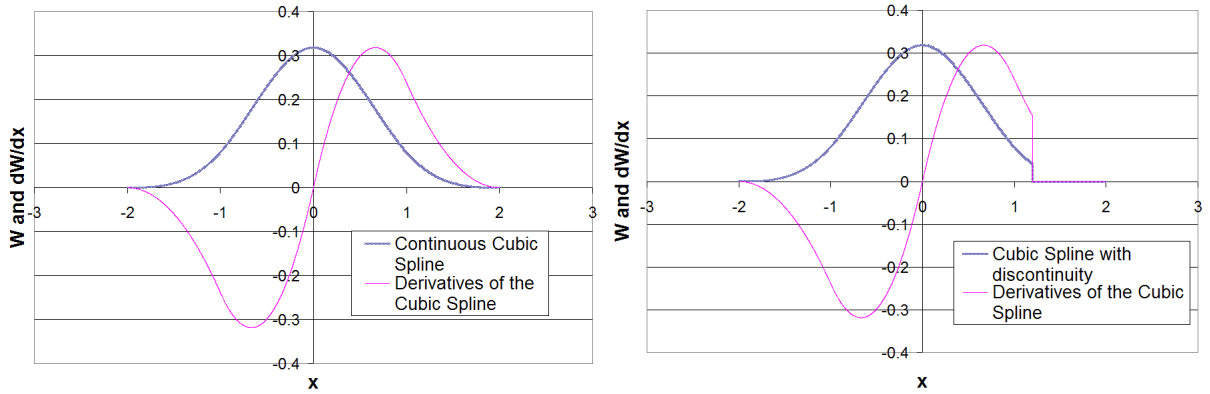


Figure 3: The one dimensional cubic spline and its derivative, left: without discontinuity, right: with discontinuity at  $x=1.2$

We will briefly describe how to implement the visibility criterion in 2D. Consider the vectors  $\mathbf{g}$  from  $\mathbf{b}$  to  $\mathbf{e}$ ,  $\bar{\mathbf{g}}$  from  $\mathbf{x}$  to  $\mathbf{b}$  and  $\hat{\mathbf{g}}$  from  $\mathbf{x}$  to  $\hat{\mathbf{x}}$  as illustrated in figure 4. For the vectors  $\tilde{\lambda}\mathbf{g}$ ,  $\bar{\mathbf{g}}$  and  $\hat{\lambda}\hat{\mathbf{g}}$ , we can write (23):

$$\bar{\mathbf{g}} + \tilde{\lambda}\mathbf{g} = \hat{\lambda}\hat{\mathbf{g}} \quad (23)$$

which can also be written as

$$\mathbf{G}\boldsymbol{\lambda} = \bar{\mathbf{g}} \quad (24)$$

with

$$\mathbf{G} = \begin{bmatrix} -g_x & \hat{g}_x \\ -g_y & \hat{g}_y \end{bmatrix} \quad \boldsymbol{\lambda} = \begin{bmatrix} \tilde{\lambda} \\ \hat{\lambda} \end{bmatrix} \quad \bar{\mathbf{g}} = \begin{bmatrix} \bar{g}_x \\ \bar{g}_y \end{bmatrix}$$

344 The straight lines  $\mathbf{g}$  and  $\hat{\mathbf{g}}$  have a common intersection  $\mathbf{s}$ , if  $0 < \tilde{\lambda} < 1$  and  $0 < \hat{\lambda} < 1$ . If  
 345  $\det \mathbf{G} = 0$ , the vectors  $\mathbf{g}$  and  $\hat{\mathbf{g}}$  are parallel. For convex discontinuities, the visibility criterion  
 346 seems to be suitable. For non convex discontinuities such as kinks and crack edges (end-points  
 347 in 2D), Belytschko et al. [6] and Organ et al. [23] proposed other methods such as the diffraction  
 348 or transparency method. Since we don't expect nonconvex discontinuities in our applications,  
 349 only the visibility criterion is applied, but the approach can easily be extended to the other two  
 350 ones as described in [6] and [23].

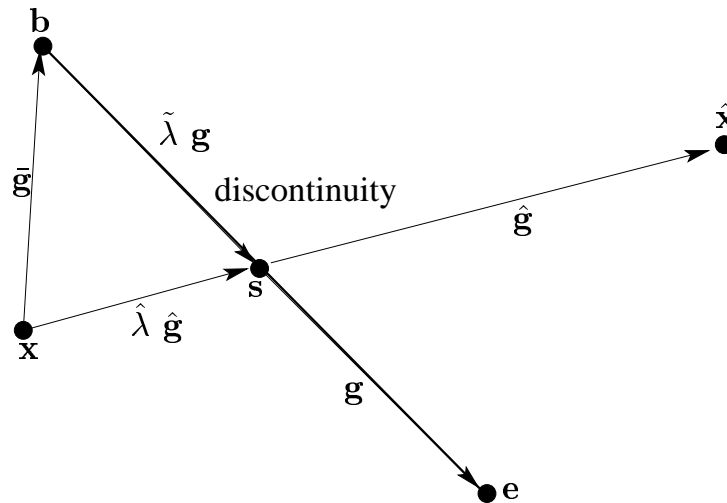


Figure 4: A crack modelled with the visibility criterion

### 351 2.3.2 The traction crack opening model

A traction crack opening model according to the EC2-model [1] is chosen. The traction depends on the crack opening  $w$  normal to the crack and the relative displacement  $u$  tangential to the crack, see figure 1. The normal traction is given by:

$$t_n = \begin{cases} f_{ctm}(1 - 0.85w/w_1) & 0 \leq w < w_1 \\ 0.15 f_{ctm} \frac{w_c - w}{w_c - w_1} & w_1 \leq w \leq w_c \\ 0 & w > w_c \end{cases} \quad (25)$$

with  $w_1 = 2G_f/f_{ctm} - 0.15w_c$  and  $w_c = \alpha_f G_f/f_{ctm}$ , where  $\alpha_f$  depends on the type of concrete and can be found in the EC2 [1] and  $f_{ctm}$  is the average of the uniaxial tensile strength of concrete according to the EC2 [1]. The fracture energy  $G_f$  is defined as

$$G_f = \int_0^{w_c} t_n(w) dw \quad (26)$$

and is a material parameter corresponding to the type of concrete, see [1]. For the tangential displacement a simple Coulomb friction model is used:

$$t_\tau = \begin{cases} \beta f_n u/u_a & u \leq u_a \\ \beta f_n & u > u_a \end{cases} \quad (27)$$

352 where we have chosen  $u_a = 2/3 w_c$  and  $\beta = 0.5$  since good agreement with some experimental  
 353 data was obtained. In the next section the coupled continuum discrete crack model will be  
 354 described in detail. A coupled damage plasticity constitutive law as described in Rabczuk and  
 355 Eibl [26] is used for the concrete before the transition to the discrete crack model.

### 356 **3 Continuum/discrete crack model**

357 The continuum discrete crack model is applied to concrete and is implemented in a meshfree  
 358 particle code. The integrals can be evaluated by different techniques (nodal integration, inte-  
 359 gration with stress points and Gauss quadrature based on a background mesh, see Rabczuk et  
 360 al. [25]). Although the general procedure is independent of the integration technique, full Gauss  
 361 quadrature creates some difficulties, e.g. the stable time step is reduced if the crack divides  
 362 the integration cell into very small subcells (see figure 9). Moreover, full Gauss quadrature is  
 363 more expensive and in this particular problem more difficult to implement. In our study we  
 364 consider only the propagation of cracks from a given crack, but we will also present an approach  
 365 to initiate a crack.

#### 366 **3.1 Criteria for crack propagation and initiation**

367 As mentioned earlier, the main idea of this method is to switch from a continuum based con-  
 368 stitutive law (stress strain law) to a discrete crack model (traction crack opening model) when  
 369 required by the constitutive law, see figure 6. For the continuum model, a constitutive model  
 370 described in [26] is adopted. A crack is initiated or propagated at particles where the PDE  
 371 loses hyperbolicity. Especially in two or three dimensions, the transition point cannot easily be  
 372 determined.

373 Several approaches such as the hoop stress criterion or the loss of hyperbolicity criterion were  
 374 developed, see Belytschko et al. [5]. A sufficient condition of a hyperbolic PDE is a positive  
 375 definite tangent modulus of the stress-strain relation. If the acoustic tensor  $\mathbf{Q} = \mathbf{n}_0 \cdot \mathbf{C} \cdot \mathbf{n}_0$  is  
 376 positive definite, hyperbolicity of the PDE is guaranteed. Belytschko et al. [5] obtained from  
 377 the loss of hyperbolicity criterion also the direction and the length of the crack, i.e. crack speed.  
 378 The hyperbolicity criterion requires that



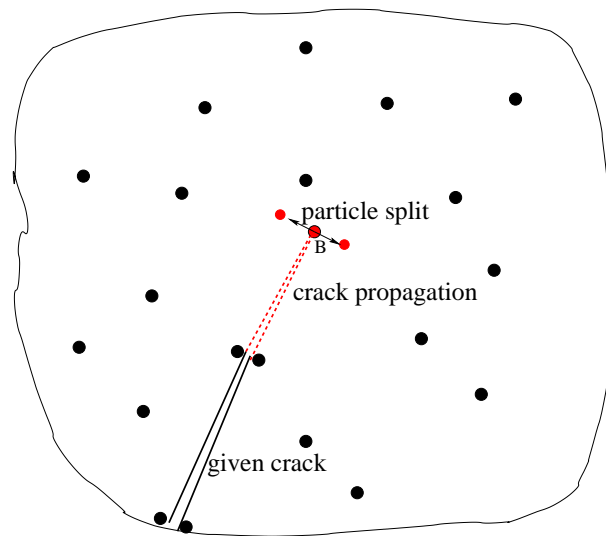


Figure 5: Scheme of crack propagation and particle split

$$e = \min_{\mathbf{n}_0, \mathbf{h}_0} (\mathbf{n}_0 \otimes \mathbf{h}_0 : \mathbf{C} : \mathbf{n}_0 \otimes \mathbf{h}_0) \geq 0 \quad (1)$$

379 where  $\mathbf{C}$  is the tangent modulus of the stress-strain curve and  $\mathbf{n}_0$  and  $\mathbf{h}_0$  are two arbitrary unit  
 380 vectors. The unit vector  $\mathbf{n}_0$  and  $\mathbf{h}_0$  are determined by a minimization procedure. The crack is  
 381 propagated perpendicular to the unit vectors  $\mathbf{n}_0$ . Sometimes problems may occur, e.g. when  
 382 the crack branches, since there may exist more than one solution in the minimization procedure.  
 383 Other criteria can be used, e.g.  $e = \bar{\sigma} - f_t$  where  $\bar{\sigma}$  is the equivalent stress of the stress tensor  
 384 and  $f_t$  is the tensile stress.

385 We have chosen a simpler approach for crack initiation and propagation as well as the  
 386 direction and length of the crack. There is a major difference between the approach here and  
 387 the approach in [13]. While in [13], the crack is propagated arbitrary through an element, hence  
 388 no remeshing is necessary, we have to refine around the crack.

389 The transition from the continuum model to the discrete crack model takes place after  
 390 exceeding a given strain value of the equivalent uniaxial stress strain curve as shown in figure 6.  
 391 According to experimental data, this is the case when the equivalent uniaxial stress strain curve  
 392 reaches its maximum tensile stress. At the beginning of the traction crack opening relation,  
 393 the relative displacements between the crack edges are zero. At this time, the traction has a  
 394 maximum  $\mathbf{t}_0^{max} = \mathbf{n} \cdot \mathbf{P}^{max}$  and is decreasing to zero during the course of the load history.  
 395 Actually, this is not remarkable, but it is mentioned because it is a major difference to other  
 396 models (see e.g. Haeusler [16]), which don't treat the crack as an internal boundary and where  
 397  $\mathbf{t}_0^{max} \neq \mathbf{n}_0 \cdot \mathbf{P}^{max}$  since the relative displacements are nonzero at the beginning of the discrete  
 398 crack approach.

399 As just mentioned, a crack is initiated or propagated if a strain threshold is exceeded. First,

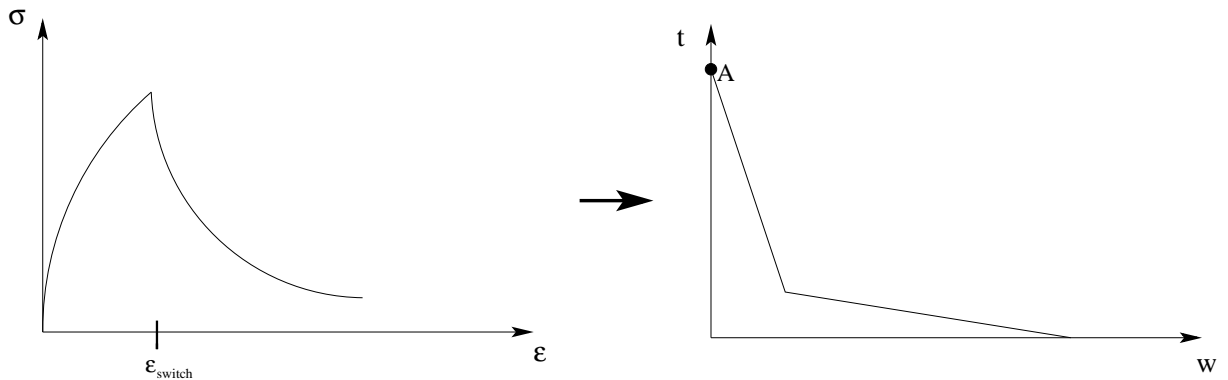


Figure 6: Switch from the continuum model to discrete crack model

400 imagine a given crack as shown in figure 5. Suppose the strain threshold is exceeded for particle  
 401  $B$  close to the crack tip. The crack will propagate in the direction of this particle. We treat the  
 402 crack by two adjacent surfaces as illustrated in figure 6. Hence, particle  $B$  is split into two new  
 403 particles. The particle split requires the recomputation of the new particle masses. They might  
 404 be computed according to a Voronoi diagram where the new crack boundary has to be taken  
 405 into account, see figure (7). More simply, the masses can be halved when a particle is split.  
 406 Since an adaptive refinement is used to obtain good resolution near the crack, the masses of all  
 407 affected particles have to be recomputed. Therefore, we compute the consistent mass matrix  
 408 after every adaptation step. The diagonal mass matrix is obtained by a row sum technique as  
 409 described in Belytschko et al. [8]. All other data are kept from the original particle.

410 The strain based criteria can also be used for crack initiation. For a mode I crack, the crack  
 411 is initiated perpendicular to the direction of the principal tensile stress for the corresponding  
 412 particle. Besides of the direction, a crack length has to be chosen. For simplicity, we have kept  
 413 the crack length constant for a given time step but other approaches are possible, too. A crack  
 414 length of  $\alpha \delta x$ , where  $\delta x = \sqrt{dx^2 + dy^2}$  and  $0 < \alpha < 1$ , seems to be reasonable. The distance  
 415 between two adjacent particles in the x-direction and y-direction is hereby denoted as  $dx$  and  
 416  $dy$ , respectively.

417 It has to be mentioned, that several problems occur if the integrals are evaluated by Gauss  
 418 quadrature. One disadvantage is that the stable time step is significantly reduced if the crack  
 419 divides a background cell into a very small cell as shown in figure 9. Implicit-explicit time  
 420 integration has to be used, see Belytschko et al. [12] or Hughes et al. [19]. The second point is  
 421 the high computational cost of full quadrature. Hence, we have chosen stress point integration  
 422 so that we benefit from the truly meshfree character. An approach for a crack propagation using  
 423 Gauss quadrature is proposed by Haeusler et al. [16] and will be used for comparison.

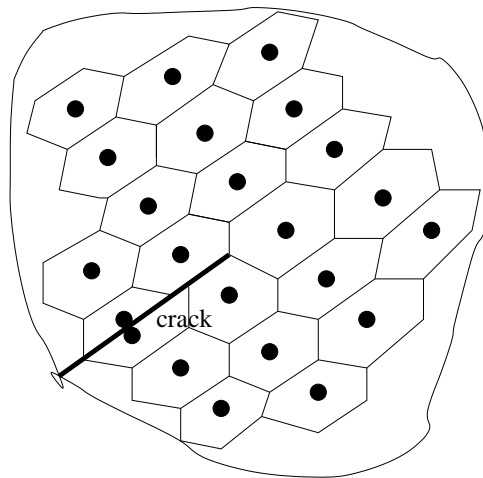


Figure 7: Voronoi cells for a particle arrangement with a crack

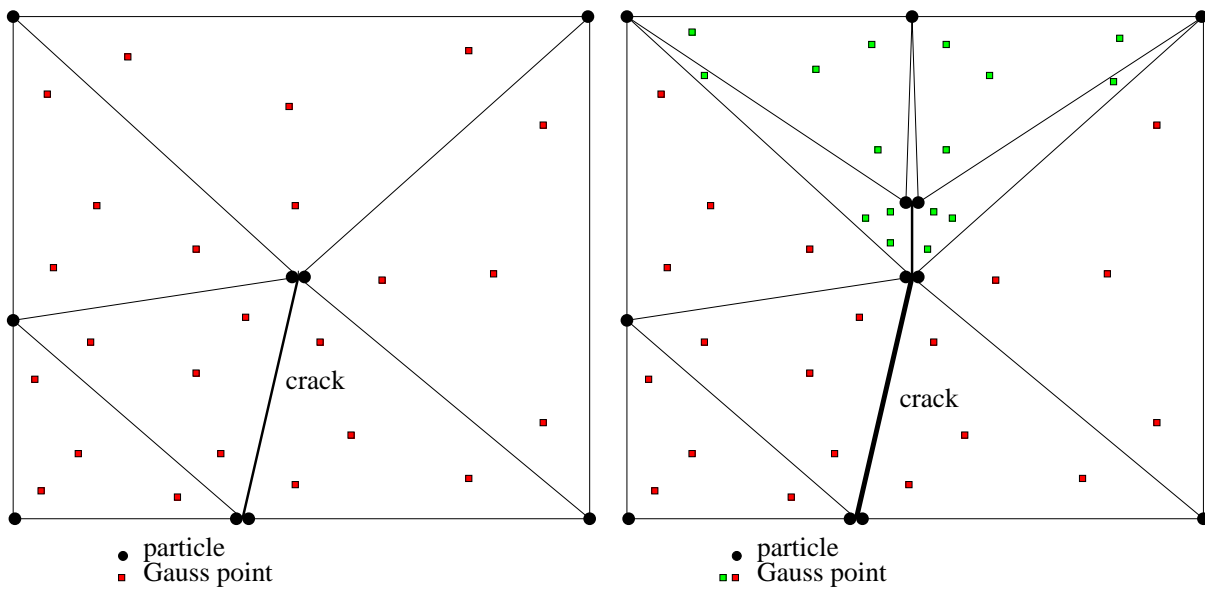


Figure 8: Crack propagation scheme and triangulation using an integration scheme based on a background mesh

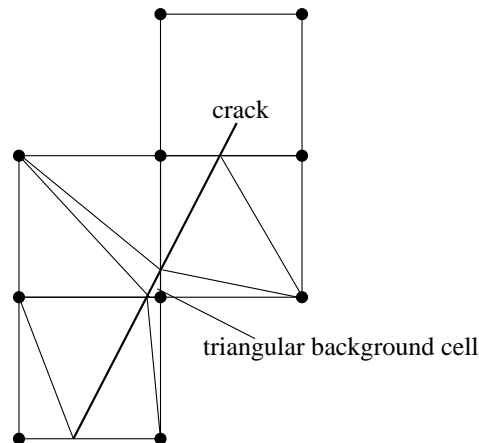


Figure 9: Stable time step for an element cut by a crack

### 424 3.2 Determination of the crack direction and length

425 To obtain good resolution near the crack and to insure that the crack is propagated in the  
 426 correct direction, high particle resolution near the crack, particularly the crack tip, is necessary.  
 427 Therefore, an adaptive refinement is used at locations with high strain gradients, that is along  
 428 the crack. The adaptive approach is explained in detail in Rabczuk et al. [24] and the description  
 429 will be omitted here. The particles are added in a rectangular pattern. However, adaptation  
 430 in only a rectangular pattern entails some drawbacks since the crack is then constrained by the  
 431 rectangular pattern and a zigzag pattern in the path of the crack can sometimes be observed, see  
 432 figure 17. If only straight cracks are considered, adequate results can be obtained when using a  
 433 high particle resolution around the crack.

434 To obtain better crack paths, an additional technique similar to the one of Hao et al. [17]  
 435 is applied. In addition to the 'usual' adaptive refinement, particles are added adaptively in a  
 436 half circle around the crack tip as illustrated in figure 10. They are distinguished from the other  
 437 particles by a superimposed  $x$ . All data is interpolated from the neighbor particles which are  
 438 denoted by a superimposed  $o$ . The stresses and strains for such particles are:

$$\mathbf{F}^x = \sum_J \nabla \Phi(\mathbf{X}^x - \mathbf{X}_J^o, h) \mathbf{u}_J^o, \mathbf{P}^{x,t+dt} = \mathbf{P}^{x,t} + \mathbf{E}_t^x : \mathbf{F}^x \quad (2)$$

439 The stresses  $\mathbf{P}^{x,t}$  are interpolated from the original particles. The stresses  $\mathbf{P}^{x,t+dt}$  can be ob-  
 440 tained directly from the total deformation tensor  $\mathbf{F}$  or by interpolation.

441 A crucial point is the choice of the radius  $r$  of the half circle. It is chosen as the minimum  
 442 particle distance  $\delta x = \sqrt{dx^2 + dy^2}$  to  $r = \alpha \min \delta x$ , with  $0.25 < \alpha < 1$ . Some results using  
 443 this technique are shown in section 4. Figure 17c and figure 17d show two results obtained with  
 444 this approach and for two values of  $\alpha$  ( $\alpha = 0.95$  and  $\alpha = 0.5$ ) compared to the 'usual' adaptive  
 445 refinement. For these examples, 37 and 73 additional particles are added on the half circle,  
 446 respectively. The particle at  $x$ , the previous crack tip, is kept and split. All other particles

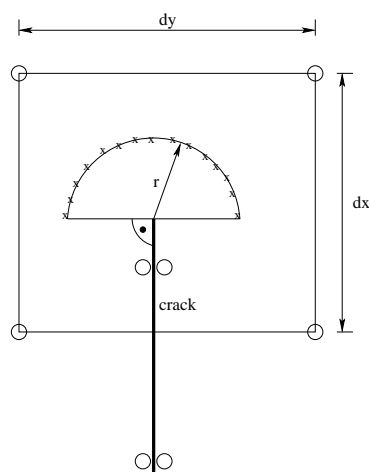


Figure 10: Scheme for the circular refinement

447 associated with this point are removed in the next step. This is necessary since with such  
 448 excessive refinement, very small particle masses and volumes would be obtained. A small value  
 449  $r$  also destroys the stable time step. The distance between the new (adaptively added) particles  
 450 and the old particles is checked, too. If the distance undershoots a given value, the corresponding  
 451 old particle is deleted. This ensures a larger stable time step.

452 For quasistatic behavior,  $r$  plays a secondary role. For dynamic behavior,  $r$  has to be chosen  
 453 carefully, since the crack speed might be influenced. To obtain an appropriate crack speed, we  
 454 divided the time step by a factor of three. Difficulties might occur for highly dynamic problems  
 455 when a structure subjected to high loads such as in an explosion.

### 456 3.3 Implementation

457 In this subsection, the implementation of the discrete crack model will be described. With the  
 458 introduction of the crack boundary and the particle split, it is possible to compute the relative  
 459 displacement of the crack edges. The relative displacements are computed in a local coordinate  
 460 system denoted by  $\xi$  and by a subscript  $l$  as shown in figure 11. The boundary particles are  
 461 assigned to a coordinate system according to their corresponding crack segment. Since we use  
 462 a total Lagrangian formulation (with a Lagrangian kernel), the coordinates of a point and the  
 463 orientation of the coordinate system stay fixed once it is computed. It is not necessary to rotate  
 464 the coordinate system as in some rotating crack models.

The relative displacements  $\delta_l = [w \ u]^T$ , where  $w$  is the normal relative displacement of the  
 crack edges, the crackwidth, and  $u$  is the tangential relative displacement according to the local  
 coordinate system, are

$$\delta_l = \mathbf{u}_l^A - \mathbf{u}_l^B \quad (3)$$

465 where the superscripts  $A$  and  $B$  indicate the 'left' and the 'right' hand side of the crack (see

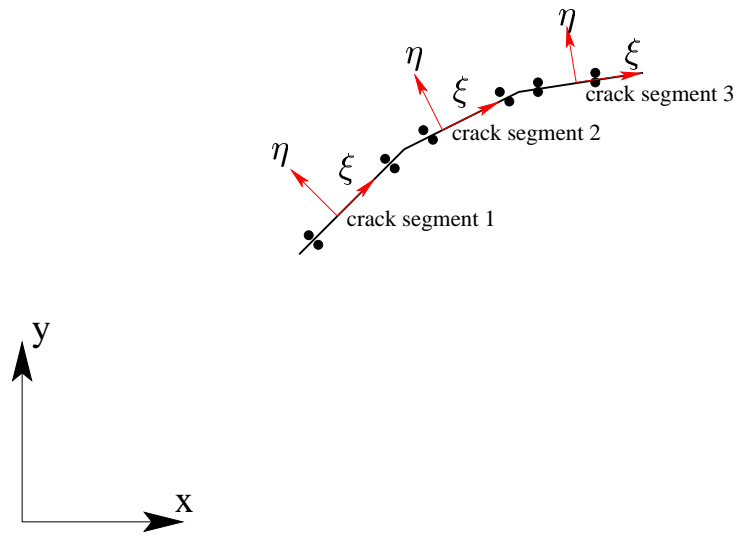


Figure 11: Relation between local crack coordinate system and global coordinate system

466 figure 1) and  $\mathbf{u}_l$  is the displacement in the local coordinate system.

467 The traction crack opening model is expressed in terms of the relative displacements in a  
 468 local coordinate system  $(e_1^0, e_2^0)$  with  $e_1^0$  tangent to the image of the crack in the undeformed  
 469 configuration and  $e_2^0$  normal to the image of the crack in the undeformed configuration. Therefore  
 470 the displacements or relative displacements  $\delta_g = \mathbf{u}_g^A - \mathbf{u}_g^B$  in the global coordinate system have  
 471 to be rotated in the local one. This can be done with the transformation matrix  $\mathbf{T}$ :

$$\mathbf{T} = \begin{bmatrix} \cos \gamma & \sin \gamma \\ -\sin \gamma & \cos \gamma \end{bmatrix}$$

472 The traction crack opening model can now be applied. The tractions in the local coordinate  
 473 system have to be transformed by  $\mathbf{T}$  into the global coordinate system where they are applied  
 474 as external forces. In the unloading case, the traction will return to the origin of the traction  
 475 crack opening curve as shown in figure 12a.

476 The transition from the tensile to the compressive regime and vice versa in a pure continuum  
 477 mechanical description is handled easily as described in Rabczuk et al. [26]. Once a discrete  
 478 crack with a crack boundary is introduced, we have to deal with contact if the crack closes.  
 479 Consider the crack as illustrated in figure 13. The crack line is formed by the neighboring  
 480 (crack boundary) particles of the corresponding crack side (left or right). We check if the crack  
 481 boundary particle on the crack line of the opposite side penetrates the two corresponding crack  
 482 lines (on the other side), e.g. contact for particle 3 is checked for segment 1 and 2 as illustrated  
 483 in figure 13. If particle 3 penetrates e.g. segment 1, contact forces to the corresponding neighbor  
 484 particles normal to the crack line are applied as shown on the RHS of figure 13, so that the  
 485 penetrating particle stays on the appropriate side at the end of the time step.  $F_1$ ,  $F_2$  and  $F_3$  in  
 486 figure 13 denote the contact forces,  $d$  is the penetration depth and  $l_3$  is the length of segment 1.

487 In our examples, no numerical instabilities were observed.

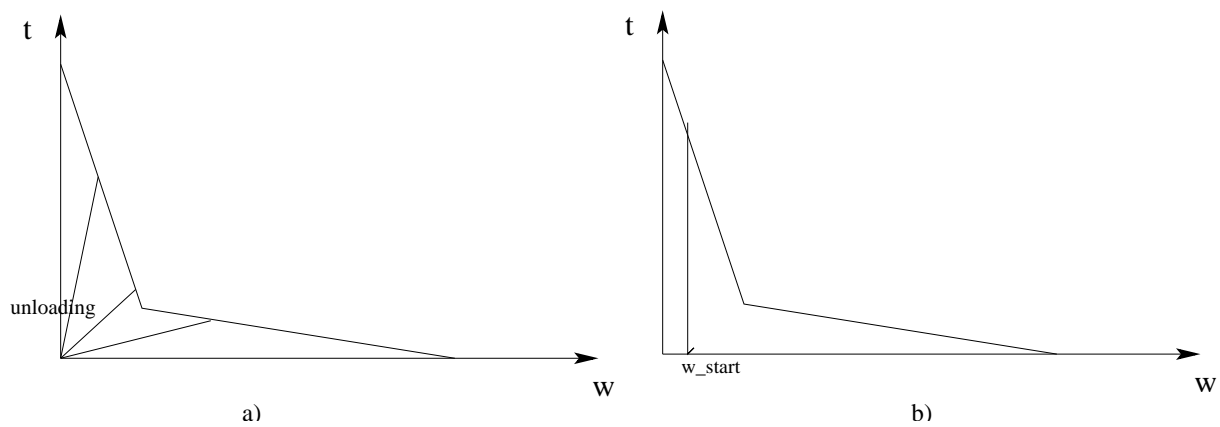


Figure 12: Discrete crack model

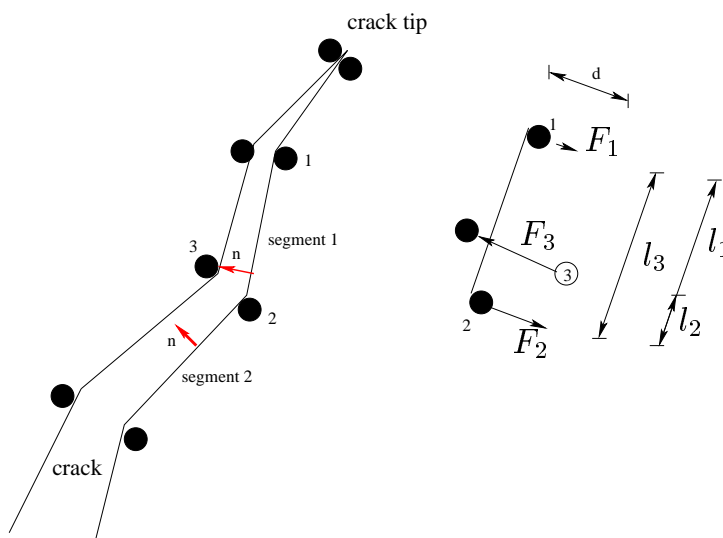


Figure 13: Imposing contact conditions on the crack boundary particles for a crack closing

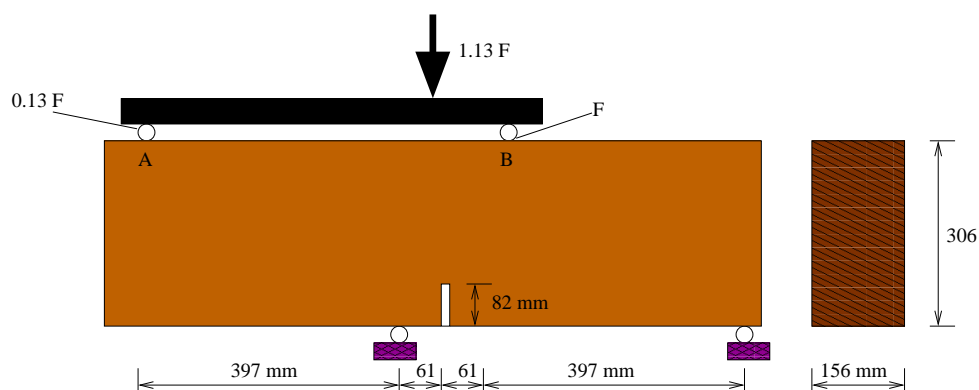
488 **4 Numerical results**489 **4.1 The Arrea/Ingraffea beam**

Figure 14: The tensile/shear beam from Arrea Ingraffea

490 The first example is the tensile/shear beam of Arrea and Ingraffea [2]. The notched beam  
 491 is loaded at two points (A and B, see figure 14). The initial elastic modulus is 28,000 MPa.  
 492 The beam fails due to a mixed tensile/shear failure. This problem is commonly used to test  
 493 constitutive laws with respect to combined failure modes.

494 The load displacement (on the RHS of the notch) curve is shown in figure 15a. In addition  
 495 to the results obtained with our discrete crack model (dcm), results with a complete continuum  
 496 damage plasticity model (cdm) (see Rabczuk et al. [26]) and experimental data are given.  
 497 Particularly the post peak behavior is modelled better by the discrete crack model than by the  
 498 continuum damage model.

499 Three different approaches are used for the discrete crack model. Model  $dcm_1$  uses the dis-  
 500 crete crack model described in Section 3 where the integrals are evaluated by a nodal integration  
 501 with stress points. No circular refinement around the crack tip is made. Model  $dcm_2$  uses also a  
 502 nodal integration and stress points for the computation of the integrals. An additional circular  
 503 refinement around the crack tip is used where the radius of the circle is chosen to be  $r = 0.95 \delta x$ ,  
 504 where  $\delta x$  is the minimum distance between particles. Additionally, the radius is decreased to  
 505  $r = 0.5 \delta x$ . Since the load displacement curve differs minimally for the two different radii, the  
 506 results for  $r = 0.5 \delta x$  are illustrated in figure 15a. For comparisons we have implemented a mixed  
 507 discrete crack/smearred crack model  $dcm_3$  as described in [16]. Model  $dcm_3$  uses a background  
 508 mesh for the integration. 25 Gauss points are used in the cells. It can be seen, that the discrete  
 509 crack models agree pretty well in the experiment.

510 The crack pattern of the beam is illustrated in figure 16a for the full continuum model and  
 511 in figures 16b and 16c for the discrete crack model  $dcm_1$  and  $dcm_2$ , respectively. First, it can  
 512 be seen, that with the discrete crack model, the crack resolution is much finer although fewer  
 513 particles were needed with the adaptive refinement. While approximately 280,000 particles were



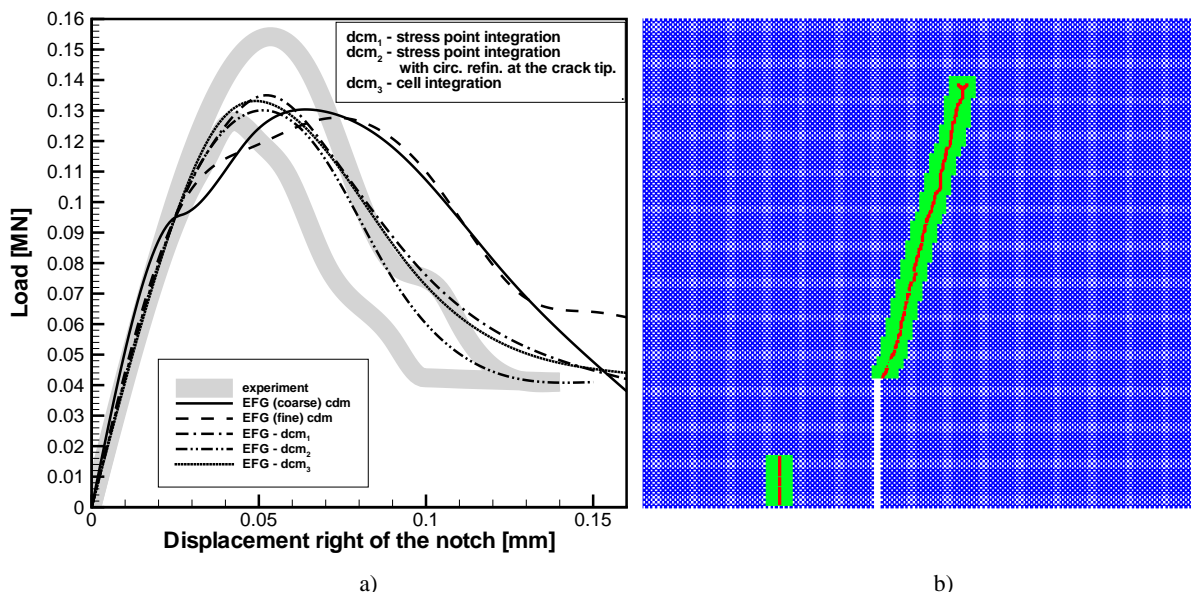


Figure 15: a) Load displacement curve, b) Crack pattern around the notch for the model  $dcm_2$

514 used in the  $cdm$ -model, we started with 30,000 particles in our discrete crack models. The  
 515 difference in the crack pattern between model  $dcm_1$  and  $dcm_2$  is small. However, for the  $dcm_1$   
 516 model the number of particles increased by a factor of 2.5 while for the  $dcm_2$  model the number  
 517 of particles were increased by a factor of 1.8. Not only the higher number of particles but also  
 518 the smaller particle separation in the  $dcm_2$  model, which diminishes the time step, increases the  
 519 computation time significantly. For this quasistatic problem, the differences between the two  
 520 discrete crack models ( $dcm_1$  and  $dcm_2$ ) are not very obvious, but it will become so in dynamic  
 521 problems.

522 With the discrete crack model, the crack widths can also be computed, which are comparable  
 523 to experimental data. In figure 15b, the beam around the notch is illustrated for the  $dcm_2$  model.

524 Cross sections for the different models are shown in figure 17. Figure 17a shows the crack  
 525 for the  $dcm_1$  model, in figure 17b, the results of the  $dcm_2$  model with a refinement radius of  
 526  $r = 0.95\delta x$  are illustrated. The red particles show the crack path. A zigzag pattern can be  
 527 observed for the  $dcm_1$  model. In the complete illustration, both computations give similar  
 528 results (see figure 16b and 16c), but more particles were necessary to obtain the appropriate  
 529 crack path when using no circular refinement. In figures 17b and 17c, the influence of the  
 530 different radii ( $r = 0.95 \min \delta x$  and  $r = 0.5 \min \delta x$ ) for the circular refinement are illustrated.  
 531 The influence of the size of the circle seems to be small in this application; this is true also for  
 532 nearly straight crack paths and quasistatic loading conditions.

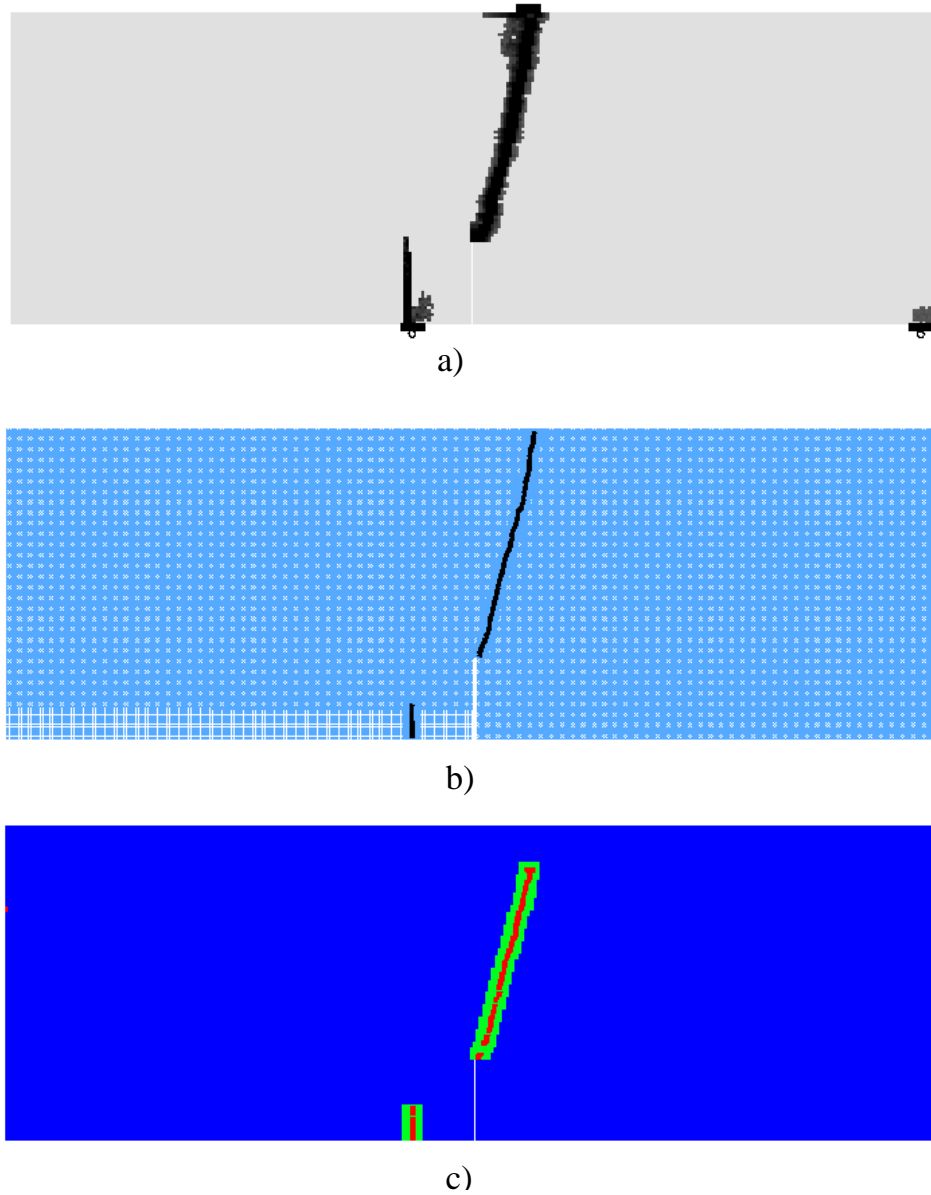


Figure 16: Crack pattern of the Arrea Ingraaffa beam for a) a complete continuum model (see [25]), b) Model  $dcm_1$ , c) Model  $dcm_2$

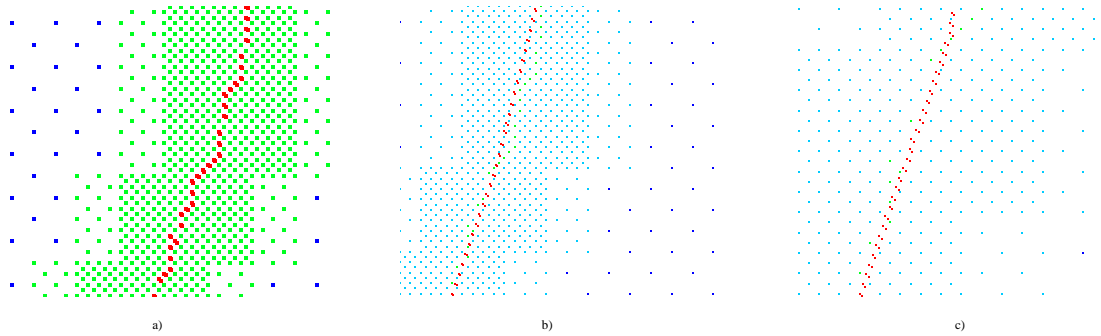


Figure 17: Crack pattern for a cutout of the beam for a) without circular refinement, b) with circular refinement for a refinement radius of  $r = 0.95 \delta x$ , c) with circular refinement with  $r = 0.5 \delta x$

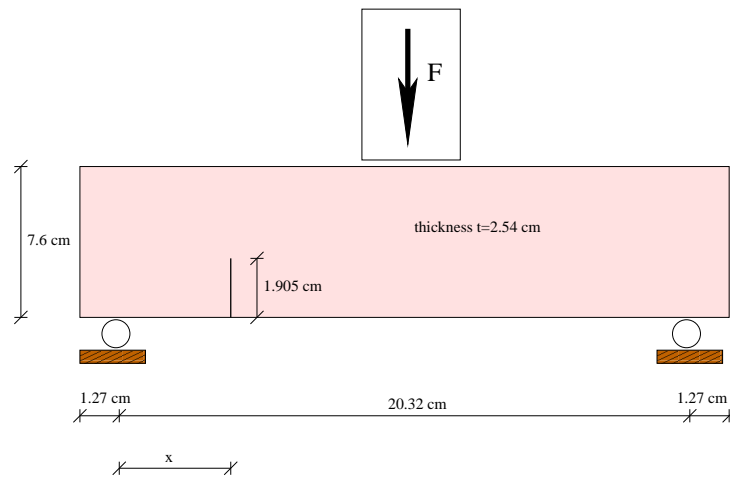


Figure 18: Test setup for the John and Shah beam

Table 1: Location of the notch

| Number | Location $x$ [cm] |
|--------|-------------------|
| 1      | 2.38              |
| 2      | 2.85              |
| 3      | 3.02              |
| 4      | 5.08              |

## 533 4.2 John and Shah beam

534 John and Shah [20] performed a series of static and dynamic experiments on notched concrete  
535 beams. Figure 18 shows the test set up. Table 1 lists the different locations of the notch. They  
536 varied the load rate and the location of the notch. The rate of loading ranged from a slow strain  
537 rate of  $10^{-6}/s$  for the quasistatic experiments to a dynamic load with strain rates of  $0.5/s$ . Two  
538 different failure modes were observed in the experiments as illustrated in figure 19. The first  
539 one is a pure mode I failure in the middle of the beam, the second one is a mixed mode failure  
540 where the crack started to propagate from the notch. The transition from the mode I to mixed  
541 mode failure depends on the location of the notch and differs for the dynamic and the static  
542 loading conditions (see figure 19). For the same location of the notch, the slope of the crack (for  
543 the mixed mode failure) for the quasistatic and dynamic loading is almost equal. We study here  
544 both dynamic and quasistatic loading. The load is applied via a boundary velocity condition  
545 given by John and Shah [20].

546 First, we focus on the notched beam number 4 ( $x = 5.08$  cm, see table 1) under dynamic  
547 loading. EFG with stress point integration is applied. Two simulations were performed, one  
548 with circular refinement (model  $dcm_2$ , see figure 20a) and one without (model  $dcm_1$ , see figure  
549 20b). The radius for the circular refinement was  $r = 0.5 \min \delta x$ . The crack has an angle of  $23^\circ$   
550 against the y-axis for the first computation (see figure 20a), which matches the experimental  
551 data pretty well, see figure 19. Without the circular refinement, an angle of  $26^\circ$  with the global y-  
552 axis is obtained, but the number of particles was two times higher than in the computation with  
553 circular refinement. At this point it should be mentioned that the experiments also exhibit some  
554 scatter. The crack path for the quasistatic computation with the circular refinement is similar  
555 to that in the dynamic loading. In figure 21 the crack path from the numerical computation is  
556 compared to the corresponding experiment. The agreement is very good.

557 Finally, we tried to reproduce the transition point of the beam failure modes as illustrated  
558 in figure 19. For the quasistatic loading, the transition point was computed quite well for a  
559 notch with a distance of 3 cm to the support, see figure 22a. In the experiments this transition  
560 point was observed for a notch with  $x = 3.02$  cm. In the dynamic loading the transition took  
561 place for  $x = 2.29$  cm which is 10% closer to the support than observed in the experiments, see  
562 figure 19 and 22b. This maybe due to neglecting time-dependent effects in our discrete crack  
563 traction law. It can be seen that the the slope of the crack path from the notch gets steeper  
564 with decreasing distance of the notch to the support.

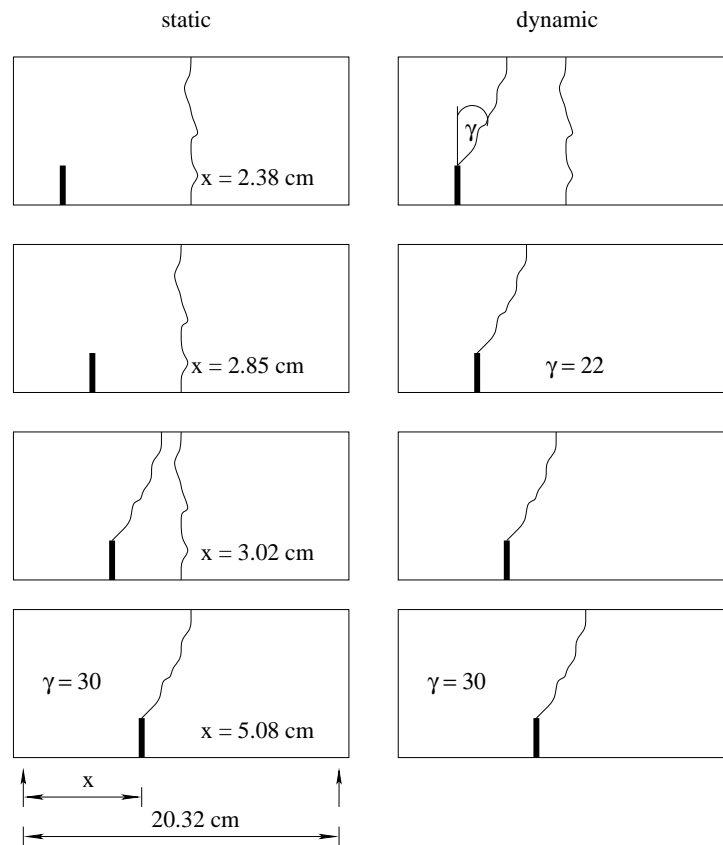


Figure 19: Crack patterns of the John and Shah [20] beam for different locations of the notch for quasistatic and impact loading

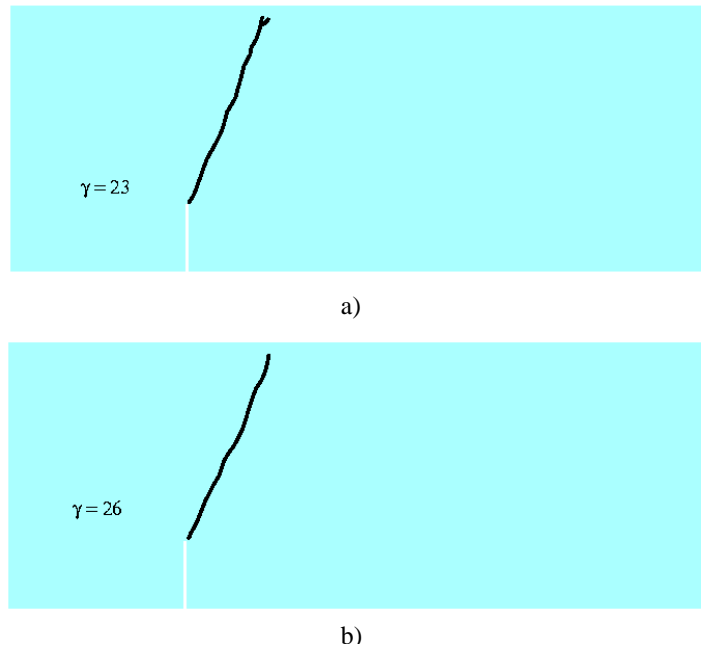


Figure 20: Crack pattern of the John and Shah beam under impact loading for a location of the notch:  $x=5.08\text{cm}$ , a) for the  $dcm_2$  model (with circular refinement), b) for the  $dcm_1$  model (without circular refinement)

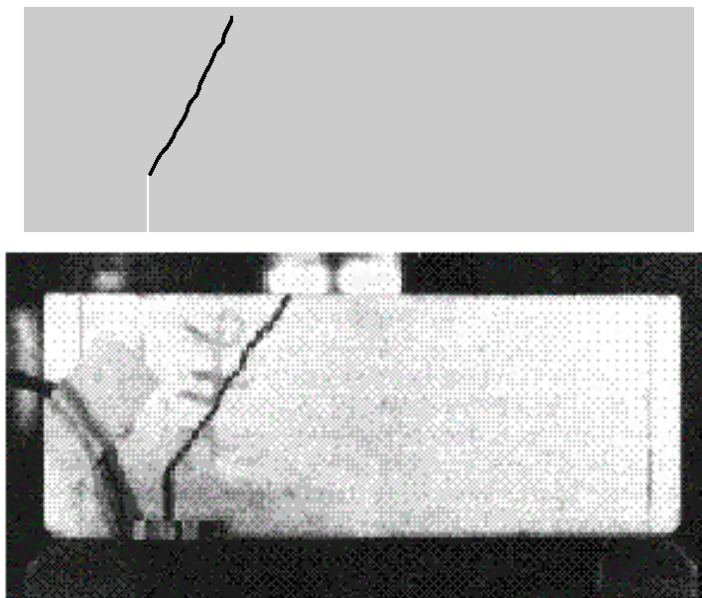


Figure 21: Comparison of the computed and observed crack pattern of the John and Shah beam under quasistatic loading

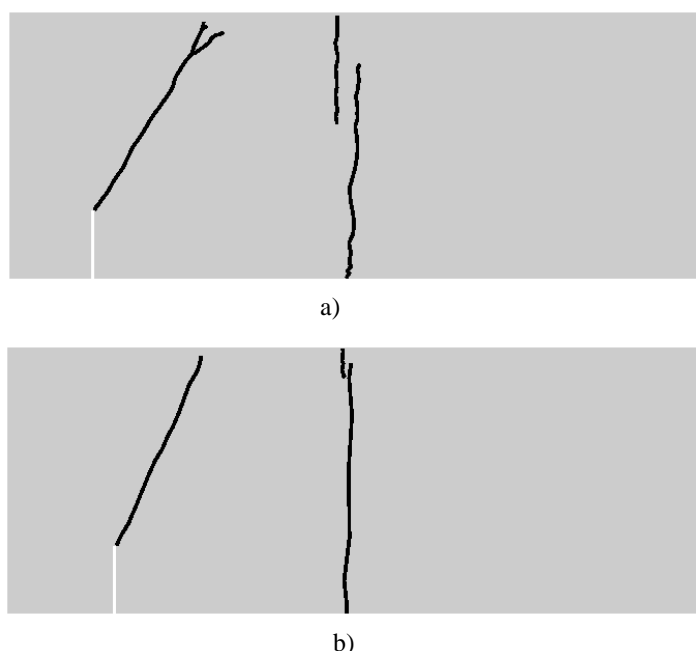


Figure 22: Computed crack pattern of the John and Shah beam near the transition in the failure mode, a) under quasistatic loading, b) under dynamic loading

## 5 Conclusion

A meshfree method that allows a transition from continuum to discrete cracks with arbitrary paths and adaptivity has been described. The discrete crack is treated as an internal boundary. The model is integrated in a meshfree particle code since meshfree particle methods are well suited for arbitrary crack propagation problems. It is easy possible to introduce boundaries and add particles adaptively. The particles were added in a rectangular pattern. Since a zigzag pattern was observed in the computation with only rectangular refinement, additional particles were added in a half circle around the crack tip; these were deleted after the crack advanced. The choice of the refinement radius  $r$  of this half circle was studied. With increasing  $r$ , an increasing crack speed was observed. Decreasing the stable time step with a factor of three was able to overcome this dependency. However, the choice of a constant  $r$  is a critical point in the computation.

The model is applied to concrete materials and mixed mode fracture problems, the Arrea and Ingraffea beam and the John and Shah beam. We were able to reproduce the crack patterns and their dependence on the notch and the load displacement curves quite well. Some discrepancies occur when the beam is loaded dynamically. One reason may be that rate effects in the traction crack opening model are not considered. These may play a significant role under high loading velocities as shown by Eibl et al. [14, 15].

583 **Acknowledgments:** The support of the Army Research Office and the Office of Naval Research are  
584 gratefully acknowledged.

## 585 References

- 586 [1] Eurocode 2: Planung von Stahlbeton- und Spannbetontragwerken. Teil 1: Grundlagen und Anwen-  
587 dungsregeln fuer den Hochbau, in Betonkalender 1993, T. II, Ernst und Sohn, Berlin, 1993.
- 588 [2] M. Arrea and A.R. Ingraffea. Mixed-mode crack propagation in mortar and concrete. Technical  
589 report, No. 81-13, Dept. of Struct. Eng., Cornell University Ithaka, N.Y., 1982.
- 590 [3] J.H. Prevorst B. Loret. Dynamic strain localization in elasto-(visco)-plastic solids, part1: General  
591 formulation and one-dimensional examples. *Computer Methodes in Applied Mechanics and Engi-*  
592 *neering*, 83:247–273, 1990.
- 593 [4] S. Bazant and T. Belytschko. Wave propagation in a strain-softening bar: Exact solution. *Journal*  
594 *of Engineering Mechanics-ASCE*, 111(3):381–389, 1985.
- 595 [5] T. Belytschko, H. Chen, J. Xu, and G. Zi. Dynamic Crack Propagation Based on Loss of Hyperbol-  
596 icity and A New Discontinuous Enrichment.
- 597 [6] T. Belytschko, M. Fleming, D. Organ, Y. Krongauz, and P. Krysl. Meshless methods: An overview  
598 and recent developments. *Comp. Meth. Appl. Mech. Engn*, 139:3–48, 1996.
- 599 [7] T. Belytschko, Y. Guo, W.K. Liu, and S.P. Xiao. A unified stability analysis of meshless particle  
600 methods. *Int. J. Numer. Meth. Engng*, 48:1359–1400, 2000.
- 601 [8] T. Belytschko, W.K. Liu, and B. Moran. *Nonlinear Finite Elements for Continua and Structures*.  
602 John Wiley and Sons, LTD, New York, 2000.
- 603 [9] T. Belytschko and Y.Y. Lu. Element-free galerkin methods for static and dynamic fracture. *Int. J.*  
604 *Solids Strucutres*, 32:2547–2570, 1995.
- 605 [10] T. Belytschko, Y.Y. Lu, and L. Gu. Element-free galerkin methods. *International Journal for*  
606 *Numerical Methods in Engineering*, 37:229–256, 1994.
- 607 [11] T. Belytschko and I.S. Yeh. The splitting pinball algorithm for contact-impact problems, computer  
608 methods in applied mechanics and engineering. 105:375–393, 1993.
- 609 [12] T. Belytschko, H.J. Yen, and R. Mullen. Mixed methods for time integration. *Computer Methods*  
610 *in Applied Mechanics and Engineering*, 17:259–275, 1979.
- 611 [13] H. Chen. Enriched finite element methods and its applications. PhD-thesis, Northwestern University,  
612 Department of Mechanical Engineering, Computational Mechanics Group,, Dezember 2002.
- 613 [14] J. Eibl. Ein neuer Ansatz fuer ein Stoffgesetz zur Beruecksichtigung grosser Dehngeschwindigkeiten  
614 bei zugbeanspruchtem Beton. *Waubke Festschrift, BMI, Schriftenreihe des Instituts fuer Baustof-*  
615 *flehre und Materialpruefung der Universitaet Innsbruck*, 9/96, 1996.
- 616 [15] J. Eibl and M. Curbach. An attempt to explain strength increase due to high loading rates. *Nuclear*  
617 *Engineering and Design*, 112:45–50, 1989.
- 618 [16] Haeusler-Combe. *Elementfreie Galerkin-Verfahren, Grundlagen und Einsatzmoeglichkeiten*. Habili-  
619 *tation, Institut fuer Massivbau und Baustofftechnologie, Universitaet Karlsruhe*, 2001.



- 
- 620 [17] S. Hao, W.K. Liu, and T. Belytschko. Modeling and simulation of damage induced crack using  
621 meshfree methods. In Proceedings of the WCCM IV, Argentina, 1998.
- 622 [18] H.K. Hilfsdorf and H.W. Reinhardt. Beton. Betonkalender 97, Teil 1, Verlag Ernst u. Sohn, Berlin,  
623 1997.
- 624 [19] T.J.R. Hughes and W.K. Liu. Implicit-explicit finite elements in transient analysis: implementation  
625 and numerical examples. *Journal of Applied Mechanics*, 45:375–378, 1978.
- 626 [20] J.R. John and S.P. Shah. Mixed mode fracture of concrete subjected to impact loading. *ASCE J.*  
627 *Struc. Eng.*, 116:582–602, 1990.
- 628 [21] S. Mindess. Fracture Process Zone Detection. *Fracture Mechanics Test Methods for Concrete*,  
629 RILEM Report 89-FMT, Chapman and Hall, London, 1991.
- 630 [22] A. Needleman. Material rate dependence and mesh sensitivity on localization problems. *Computer*  
631 *Methodes in Applied Mechanics and Engineering*, 67:69–86, 1988.
- 632 [23] D. Organ, M. Fleming, T. Terry, and T. Belytschko. Continuous meshless approximations for  
633 nonconvex bodies by diffraction and transparency. *Comp. Mech.*, 18:225–235, 1996.
- 634 [24] T. Rabczuk and T. Belytschko. Adaptivity in explicit meshfree particle methods. submitted.
- 635 [25] T. Rabczuk, T. Belytschko, and S.P. Xiao. Stable particle methods based on lagrangian kernels.  
636 submitted to *Computer Methods in Applied Mechanics and Engineering*.
- 637 [26] T. Rabczuk and J. Eibl. Simulation of high velocity concrete fragmentation using sph/mlsph. *Int.*  
638 *J. Numer. Meth. Engng*, 56:1421–1444, 2003.
- 639 [27] Schmidt-Hurtienne. Ein dreiaxiales Schaedigungsmodell zur Beschreibung des Dehnrateneffektes von  
640 Beton. Dissertation, Institut fuer Massivbau und Baustofftechnologie, Universitaet Karlsruhe, 2000.